

Chapter 1

Microscope Design for Simultaneous Measurements on Plasmonic Tips

Atomic force microscopy (AFM) tip experiments are performed in a custom-built microscope for optical spectroscopy with simultaneous force and electronic measurements. The microscope is fully automated¹ and capable of running a variety of experiments, primarily to study the optical response of tips. Its primary function is to take the tips of two opposing AFM probes, align them into a tip-to-tip dimer geometry and demonstrate nm-scale precision spatial control. Using such a setup, the plasmonic behaviour of both individual and coupled tip systems can be investigated. In this chapter the principles behind the operation and design considerations of the microscope system are discussed in depth, with sections split between the mechanical and optical design of the microscope followed by integration of the electronics and AFM module for force measurement.

1.1 Mechanical Design

To gain insight into the behaviour of realistic metallic nanostructures, along with any chemical treatments or potential applications, requires experiments be carried out in ambient conditions. Measurement of the physical properties of two nanostructures on the sub-nm scale in ambient conditions is a difficult challenge. For a microscope to be able to perform such measurements requires many careful considerations, the result of which is a compact experimental platform resistant to both vibrations and thermal effects.

The most important parts of any microscope are the sample stage and objective lens. For stable optical measurements these have to be locked together and mechanically referenced in a symmetric configuration to prevent mechanical or thermal drift between the sample of interest and the focal spot of the source. The short mechanical reference distance in an inverted microscope design provides the best stability and the microscope platform (Figure 1.1) is designed based on this concept. Mechanical drift is minimised by maintaining a close reference

¹A custom Python application used to control the microscope and all experiments

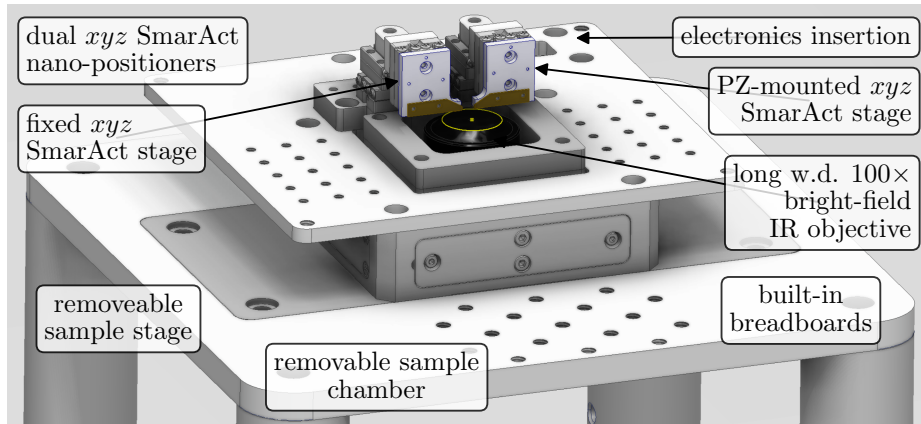


Figure 1.1: Mechanical design of the microscope. The main features of the inverted microscopy platform are highlighted, including two independent nanopositioners, one with piezo control, situated on a removable breadboard plate above the focus of an objective. Breadboard holes enable the mounting of optomechanics close to the sample. The top plate features a sealed lid with gas inlets for environmental control.

point between the sample and the objective. In this case the sample stage is tightly potted into a top plate from which the objective is screwed so that any vibrations between sample and objective occur in phase. Thermal drift is minimised by exploiting symmetry such that any expansion is around the objective and that all mechanical plates expand at the same rate. Cast aluminium is used for plate construction for its lower coefficient of thermal expansion compared to regular aluminium, whilst still remaining cheap and easily machinable compared to steel or titanium. The overall microscope platform is constructed 200 mm above the table on 1.5" diameter steel posts. The 200 mm height maintains stability without the need for cross-linking and is spacious enough to accommodate optics. The microscope platform and all important optics are mounted onto an anti-vibration stage to reduce vibrations. All optics are mounted in either cage or lens tube, held 5 mm off the table and locked together, for stability.

The typical experiment sample setup is shown in Figure 1.2a. Samples are mounted onto either of two 3-axis slip-stick translation stages with 12 mm of travel and fine piezo control (SmarAct GmbH, SLC-1720-S w/ MCS), of which one is mounted onto a 3-axis piezo translation stage (PI GmbH, PI-733.3CD) for finer motion control. The top platform design is modular and easily removable, with a tight-fitting socket precise enough to relocate the sample stage to within 10 μm after removal. Multiple adapters are used to mount different samples onto the stage. A cover slip holder is used for nanoparticle characterisation while AFM chip holders (Figure 1.2b) are designed to mount tips. AFM probe mounts are made from machinable glass-ceramic (MACOR, Corning inc.) in order to prevent thermal expansion (good coefficient of thermal expansion $\alpha_{T,\text{MACOR}} = 9.3 \times 10^{-6} \text{ K}^{-1}$, compared to other machinable materials' $\alpha_{T,\text{aluminium}} = 23.1 \times 10^{-6} \text{ K}^{-1}$, $\alpha_{T,\text{titanium}} = 8.6 \times 10^{-6} \text{ K}^{-1}$ or $\alpha_{T,\text{ABS}} = 30.4 - 73.8 \times 10^{-6} \text{ K}^{-1}$ [1]) and to electrically insulate the mounts from the nanop-

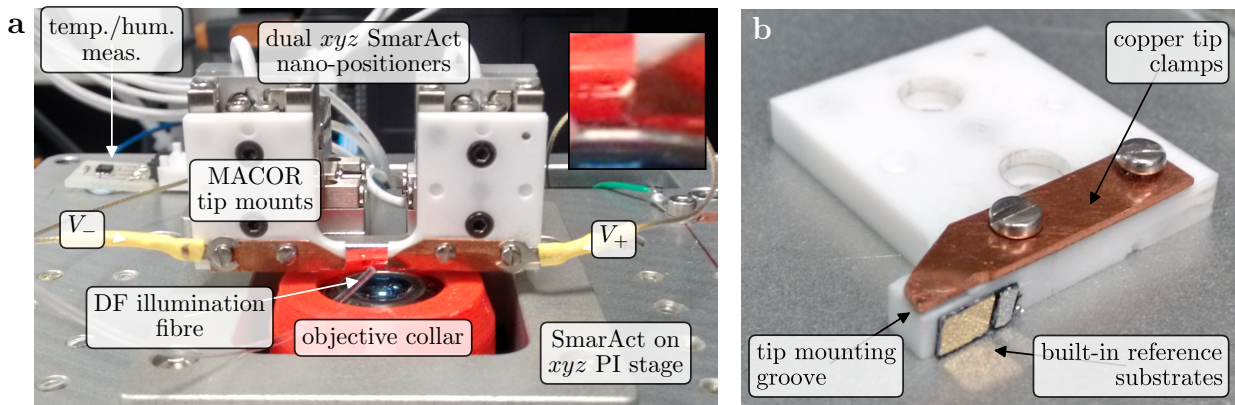


Figure 1.2: Design of the dual tip microscope stage. Images are annotated with the key design features incorporated into the sample stage. (a) Design of the dual tip mount stage and dark-field illumination mechanics. Each nanopositioner with tip mount clamp is connected to an external electronic circuit. A 3D-printed, plastic collar is attached to the objective, holding a 1 mm diameter optical fibre for dark-field side-illumination of tips. A temperature and humidity sensor is attached to the back of the plate for environmental monitoring when the chamber is sealed. (b) Design of the tip mounts. Tips are placed in a rectangular groove in the insulating MACOR plate and held in place by an angled Cu clamp. Electrode solder tags are screwed down onto the clamp to electrically contact the tip. Mirror substrates are stuck onto the bottom of the mount to provide an easily accessible, in-situ spectral referencing point for incident illumination.

sitioners. The copper clamps holding the AFM probes are contacted to enable biasing of the junction between tips and measurement of the current through the junction.

The grounded experimental chamber is sealed to control the gas environment (switchable between a line containing air bubbled through water and a nitrogen line to control humidity) and act as a Faraday cage to reduce electromagnetic interference (EMI) incident on the sample. The chamber is equipped with a low pressure, one-way valve and a needle valve to control the gas flow. Silencers are attached to the gas inlets with a foam surround to prevent air currents. The presence of a sealed chamber is enough to stabilise the sample against external air currents and help maintain a constant thermal equilibrium around the sample. A low magnification basic microscope, constructed from a small CCD, is attached to the roof of the chamber to aid alignment of samples with the objective focus. Metal contacts connect the roof to the grounded base to form the Faraday cage. Optical windows on the sides of the chamber are used to insert secondary lasers perpendicular to the objective axis, used primarily with the AFM module. They also allow for external monitoring of the stage positions from the side.

1.2 Optical Design

Dark-field (DF) spectroscopy is the primary optical method used to study plasmonic nanosstructures, in which samples are illuminated at high angles with reflections filtered to collect only low-angle scattering from the focal plane. This microscope employs two kinds of DF mi-

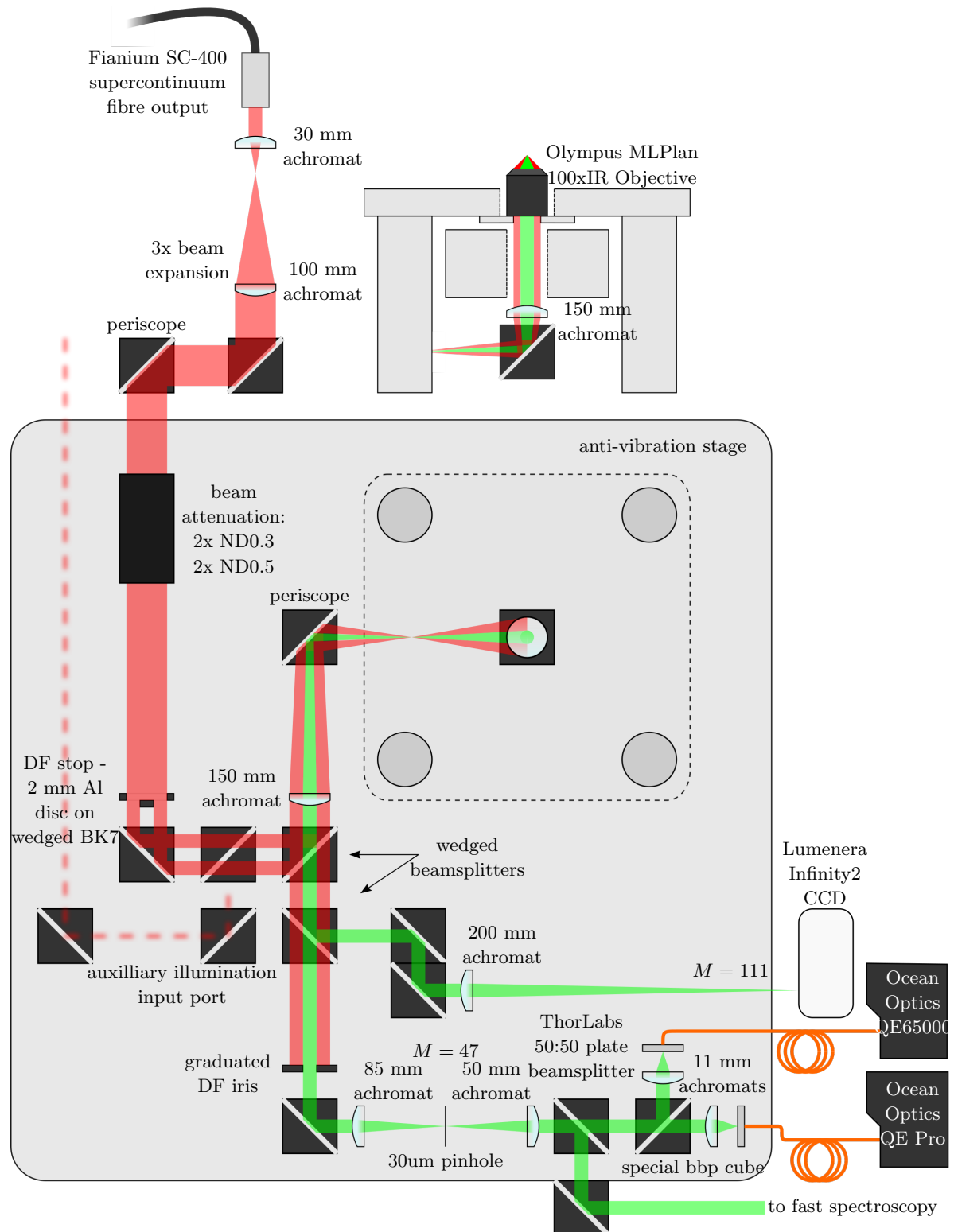


Figure 1.3: Diagram of the full optical layout and specification of the microscope.
All optics are accounted for except for silver periscope mirrors, which transfer the beam between platforms of differing height.

croscopy - conventional DF imaging using a side-illumination fibre and supercontinuum (white light) laser DF spectroscopy.

The optical design employs the concept of reimaging spatial filters into the correct planes for efficient DF spectroscopy, leading to a compact design. Employing reimaging means that beams are not necessarily required to propagate exactly along the optical axis, minimising the number of long, empty beam lines, typically used for alignment. By reimaging the front and back focal planes of the objective, spatial and Fourier k -space filters are placed in the corresponding planes, ensuring optimum filtering performance and minimal aberration. A detailed schematic of the microscope platform and the surrounding optical bench layout, containing the specifications of all optics used, is found in Figure 1.3.

Both image and Fourier planes are set through careful placement of each set of lenses. The required minimum degrees of freedom for beam alignment are accounted for by mirrors placed in the focal and Fourier planes. Those in Fourier planes change the position of the beam without affecting its shape, whereas those placed in focal planes only change the beam shape without shifting the position in the objective focus.² The position and shape of the beam are therefore independently adjustable, greatly simplifying beam alignment. This advantageous technique results in a high beam quality, and, as a direct result of the lack of long, iris-containing beam lines, a compact microscope.

A long working distance objective is required for imaging and spectroscopy of tips. Additionally, a large numerical aperture (NA) is required to properly study nanostructures as it means light is collected across a large acceptance angle with a small focal length and large magnification. A bright-field (BF) long working distance IR objective (Olympus LMPlan 100 \times IR, 0.8 NA) is used to access wavelengths above 700 nm, for which the more convenient DF VIS objectives (Olympus LMPlan 100 \times BD) exhibit a sharp cutoff.³ A DF illumination/collection configuration is necessary for spectrally studying scattered light from a nanostructure. Since DF illumination is not supported on BF IR objectives, light needs to be brought in externally in a side-illumination geometry to image samples. A 3d-printed objective collar is used to hold a 1 mm diameter optical fibre \sim 1–2 mm from the sample, outside of the objective collection angle, to which a cold white LED is fibre coupled. The fibre is fed through a breadboard hole in the top plate and sealed so as to preserve the environmental chamber integrity. The fibre outputs a broad cone of light which illuminates samples over a large area.

Use of a ultra-high brightness supercontinuum laser source (Fianium SC-400, 4 W, 480–1750 nm) enables single nanostructure spectroscopy with exposure times around 10–50 ms. The beam is expanded to fill the back aperture of the objective and apertured into a ring to mimic DF illumination using a DF disc stop. The inner diameter of the ring is set at 2 mm and the outer diameter is set by the back aperture of the objective, in this case 4 mm. This

²Diagrams indicating the principles of beam alignment using reimaging are found in the appendices.

³A comparison of the two available 100 \times objectives is found in the appendices.

technique is a pseudo-DF method denoted supercontinuum dark-field (SDF). To prevent laser damage to samples the incident power is heavily attenuated. Reflective neutral density filters totalling ND 1.6 (2.5% transmission) are placed in the beam line to reduce the initial incident power. The majority of the incident power is lost at the DF stop. Further attenuation results from the 10:90 (R:T) beamsplitter used to relay the laser into the microscope. At this point the total power is reduced to 1 mW, as measured on a bolometer (Coherent, inc.) behind the objective.⁴ Whilst the power is seemingly low and comparable with high-brightness incoherent light sources, the focussing ability of the single mode laser results in an intense, diffraction-limited, white light focus not possible with incoherent sources. For an assumed broadband spot size around 1 μm the focal intensity is $\sim 10^5 \text{ W cm}^{-2}$ between 480–1700 nm.

The incident light is apertured and reimaged directly onto the back focal (Fourier) plane of the objective, as opposed to aperturing close to the objective back aperture. This prevents diffractive artefacts in the conjugate plane of the collected light. The ring aperture means that the focus is illuminated only at high-NA as with conventional DF spectroscopy. Scattered light is then filtered by a DF iris in the return beam path to remove any signal contribution from reflected, high-NA illumination. Reimaging allows both the DF iris and stop to be located away from the objective for convenient access and easy adjustment. Alternative designs using optics mounted at the objective back aperture do not benefit from having the stop and iris in conjugate planes and may require motorised irises if not accessible by hand. For this experiment a simple graduated dark-field iris is sufficient for external use to filter the collected light signal.

Since incident power is not an issue, and in many cases requires significant attenuation, the microscope is optimised for efficient collection. The 10:90 beamsplitter used for laser input means only 10% of collected light is lost when returning back through the main microscope arm. Furthermore, all optics in the system are optimised for light between 500–1100 nm.⁵ The angle-dependent Fresnel coefficients of the glass used in all optics components mean that *p*-polarised light is favoured during transmission throughout the microscope collection path.⁶ A 90° turning periscope is placed after the first reimaging lens to reverse the linear polarisations of light so that the stronger *p*-polarisation component is orientated along the tip axis.

Subsequently, collected light is split into imaging and spectroscopy paths using a second (50:50) beamsplitter placed before the DF iris. CCD imaging is both used to align and characterise the laser focus and to centre samples onto the targeted laser illumination spot. Sample imaging uses light collected from the scattered white side-illumination LED light to

⁴Power characterisation found in the appendices.

⁵Broadband optimisation is achieved via exclusive use of Ag mirrors, Edmund Optics VIS-NIR AR coating on lenses, COMAR NIR and ThorLabs visible or visible-NIR coated beamsplitters.

⁶All beamsplitters have some degree of polarisation sensitivity due to Fresnel coefficients of the glass used. Reflectance can be a factor of 2 different between orthogonal linear polarisations. For comparison of glass reflectances and Fresnel coefficients see the appendix.

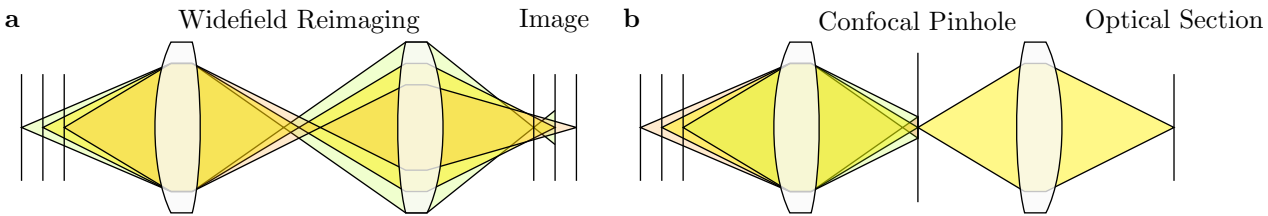


Figure 1.4: Diagram of optical sectioning in confocal microscopy. (a) Out of focus light from nearby reimaged focal planes leads to blur and a decrease of resolution in images. (b) Images spatially filtered in the focal plane by a confocal pinhole localise light from only a select volume that is sufficiently focussed to pass through the pinhole aperture.

produce DF images whereas the laser light is not DF-filtered in this path. Images are magnified $111\times$.⁷ Light passing along the spectroscopy path is DF-filtered to remove any contributions to the scattering signal from reflected light. A graduated iris is used to remove the 2 mm outer-ring of the returning beam. The iris is placed in the image plane of the DF stop for the most accurate filtering and optimum performance. The two beamsplitters present before the DF iris are wedged to prevent ghost images, which transmit through the closed iris and create spectral artefacts. However, the 5 mm thickness of wedged beamsplitters means increased dispersion and the limited availability of broadband AR coatings results in reduced reflectance in the NIR. Additionally, the DF-filtering process only works to remove light reflected out at the same angle. Angled samples (such as the facets of tips) can reflect light into the low-NA collection, creating spectral artefacts. It is for this reason that the flat tip facets are even visible in a dark-field configuration.

1.2.1 Confocal Localisation of Spectra

Since the laser focusses to a diffraction-limited spot on the sample, spectra are collected from a small sampling volume. This single mode input forms the first component of confocal localisation. Further spectral localisation is achieved by confocally filtering the image plane after the DF iris using a $25\text{ }\mu\text{m}$ pinhole to collect light from only the central focal spot. Only light in focus on the pinhole may pass through it. By rejecting out of focus light the image becomes an optical section with a tighter depth of focus. The size of the pinhole sets both the lateral and axial width of the transmitted light and leads to both spatial masking and optical sectioning in the objective-sample plane, as shown in Figure 1.4. Spectra are therefore acquired from a localised sampling volume, as set by the location of the $47\times$ demagnified pinhole image. The location of this spatial mask image in the objective focus is controlled by a mirror before the confocal filtering array. A slip-in small CCD is used to image the Fourier plane before and after confocal filtering to check pinhole alignment. Since the depth of focus scales as M^2 (or NA^2) the placement of the pinhole along the beam path is not critical. Choice

⁷Magnification is calculated by the ratio of focal lengths, $M = f_2/f_1$.

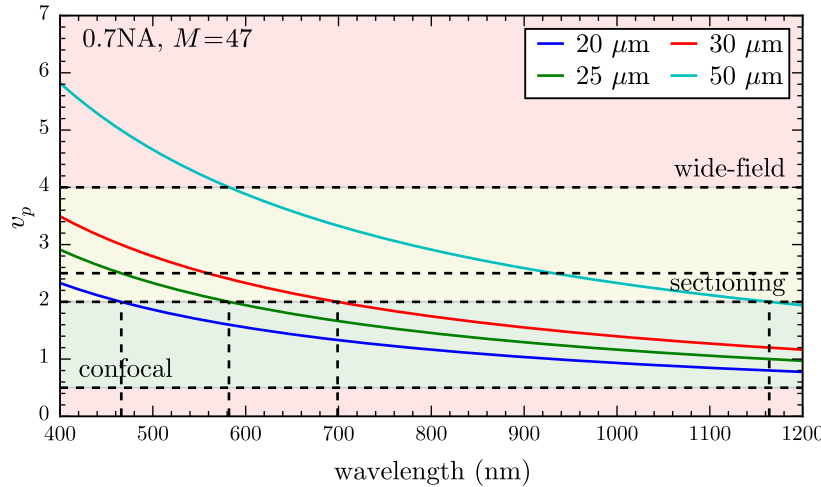


Figure 1.5: Optimum confocal pinhole size across the visible-NIR spectrum. A $25\text{ }\mu\text{m}$ pinhole is chosen for most experiments. Confocal performance is then achieved above 500 nm .

of pinhole diameter, however, is important.

Confocal filtering not only improves image contrast but also improves upon the wide-field, diffraction-limited resolution by up to a factor of $\sqrt{2}$, depending on pinhole diameter, at the cost of image brightness [2–5]. This stems from the removal of higher diffraction orders by the pinhole. The resolution of a microscope is often quantified using the Rayleigh criterion - the distance from the maximum of the PSF (expected to be an Airy function) to the first minimum [6]. A decrease in the Rayleigh criterion of diffraction-limited resolution is expected, going from $r_{\text{lateral}} = 0.61\lambda/NA$ down to $r_{\text{lateral}} = 0.44\lambda/NA$ at best. Decreasing the pinhole diameter therefore not only decreases the optical section thickness but also the minimum resolvable lateral distance to a certain extent.

For a realistic detector aperture the collection point spread function (PSF) is convoluted with its aperture function, D_p , giving an image PSF $I = |h_1|^2(|h_2|^2 * D_p)$ [7]. The resulting resolution depends on a quantity v_p , the detector width, which can be related to the actual pinhole diameter, d_p , through [7],

$$v_p \geq \frac{\pi d_p NA}{M \lambda}. \quad (1.1)$$

The full-width half-maximum (FWHM) of the PSF retains the full, $\sqrt{2}$ improvement if $v_p \leq 0.5$, but this leads to a significant loss in brightness. An increased resolution is still in effect until $v_p \geq 4$, at which point the wide-field behaviour is recovered. Practically, $v_p \leq 2$ for optimal lateral resolution and $v_p \leq 4$ for optimal depth resolution. Optimising for $v_p = 2$ means that for a 0.7NA , $M = 47$ system $d_p/\lambda \leq 43$, i.e. $21\text{ }\mu\text{m}$ at 500 nm and $47\text{ }\mu\text{m}$ at 1100 nm . A plot of v_p across the visible-NIR spectrum for a number of pinholes is shown in Figure 1.5, highlighting the relevant confocal regimes. For a given pinhole size that acts confocally in the visible, the intensity of some NIR wavelengths will be reduced since v_p drops

below 1, however this loss is acceptable to maintain higher resolution in the visible region of the spectrum. A 25 μm pinhole size is determined to be optimal in this microscope based on this analysis and the range of available pinhole sizes.

Once filtered only the spectral content of the beam is of interest rather than the image so strict adherence to conjugate planes is no longer necessary. The beam is split 50:50 into two signals, with one going to the benchtop spectrometers and the other to a fast spectroscopy path.⁸ The benchtop spectroscopy signal is further split into linear *s* and *p* polarisation components using a broadband polarising beamsplitter cube (Melles-Griot 300–1100 nm). Broadband polarisers (Thorlabs 500–1500 nm) oriented along the *s* and *p* axes are placed at the cube output ports to increase the extinction. Each polarised signal component is then finally focussed into multi-mode fibres, using short focal length (11 mm) lenses to achieve a spot size smaller than the fibre core. 100 μm fibre core is used instead of 50 μm to reduce laser speckle in spectra since the confocal pinhole diameter already localises the signal. The spectral signal from each of the fibres is recorded using TE-cooled, benchtop spectrometers (Ocean Optics QE65000 and QE Pro) with integration times between 10–50 ms. The sensitivity of the Si detectors in the spectrometers drops off beyond 900 nm, imposing a limit to detectable signals of around 1100 nm. The supercontinuum laser imposes a 480 nm spectral short wavelength cut-off, resulting in an overall effective measurement window of 500–1100 nm.

Measured spectra are background-subtracted, to remove dark counts, and referenced to the spectral density of the supercontinuum illumination as transmitted through the microscope optics. Use of the intense supercontinuum source means low integration times below 20 ms are sufficient to near saturate the spectrometer for a high quality signal to noise. The high brightness of the supercontinuum laser at these exposures also means that the relative intensity contribution from external light sources is negligible. The coherence of the supercontinuum laser means that conventional referencing using scatter from a white diffuser to map the illumination spectral density is not possible. Instead, reflections from thin, reflective substrates attached underneath the piezo-mounted tip mount are used as a reference. Different substrates are used depending on the sample. For metallic samples the substrate is matched to the metal so only structural spectral features are observed. Otherwise either a Ag mirror or glass slide are sufficient for referencing as they provide relatively flat reflectances across the visible-NIR spectrum. The DF iris is kept fully open during reference acquisition to ensure the full spectral content of the incident beam is measured and to avoid introducing referencing artefacts. As optics are very rarely broadband between 500–1100 nm, all non-essential pathways are closed when acquiring spectra to prevent artefacts. Back reflections off lenses are found to superimpose a weak duplicate of the illumination spectrum onto spectra since the reflections are translated in *k*-space and are therefore not completely filtered by the DF iris.

⁸The fast spectroscopy technique is developed and implemented but otherwise not used in any experiments in the current project. For this reason it's operation is omitted from this work.

1.2.2 Characterisation of Microscope Performance

During most experiments the power incident on samples is kept below 1 mW corresponding to a focal intensity of $\sim 10^5 \text{ W cm}^{-2}$. This is used to maintain sufficient signal quality whilst preventing damage or destructive changes to nanoscale Au samples (typically 50 nm Au coatings). Beam profiling, the study of the beam shape through the focal volume, is used to characterise beam propagation in the microscope and determine its ability to collect DF spectra. Profiling is carried out using focal scans of both light reflected from a Ag mirror and light scattered from an 80 nm AuNP, measured simultaneously on a CCD and a spectrometer. The CCD is used to laterally profile the beam through the focus while the spectrometer characterises the confocal profile and spectral distribution of the light. Both the illumination and collection pathways are profiled. The illumination pathway is profiled using the DF-filtered supercontinuum beam while one of the collection fibres is removed from its spectrometer and coupled to a 532 nm single mode laser in order to profile the collection pathway.

Figure 1.6 shows both the lateral focal spot on the CCD and relevant cross sections along the optical and focal axes for both the illumination and collection optics, along with depth-profiling using broadband-integrated spectra. Figure 1.6a shows the beam structure in the focus. The single mode fibre output exhibits the characteristic Airy profile expected of a Gaussian beam while the ring aperture of the supercontinuum beam leads to more power concentrated in the outer rings of the focal pattern (Figure 1.6b). The measured FWHM of the collection beam is $(460 \pm 20) \text{ nm}$ with a beam waist ($1/e$ width) of $(540 \pm 20) \text{ nm}$. The $47\times$ demagnified image of the $25 \mu\text{m}$ pinhole is expected to be 530 nm. The focal radius of a single mode Gaussian beam (the beam waist) is given by $w_0 = \lambda/\pi NA$, which results in a collection NA of 0.62 ± 0.02 . Measurement of a Rayleigh criterion length of $(530 \pm 20) \text{ nm}$ indicates the beam is focussed through $0.61 \pm 0.02 \text{ NA}$. Uncertainties on these calculations of the NA are small since the 532 nm wavelength is well known. Both calculations of the NA only partially agree due to beam focussing at the diffraction limit and both show a collection half-angle of $(38.0 \pm 0.5)^\circ$.

The axial cross section of beams (Figure 1.6c) shows the focussing of the high angle ($0.64\text{--}0.8 \text{ NA}$, $40\text{--}53^\circ$ incident angle) supercontinuum ring. The boundary between incident and collection beams is measured to be around 0.62 in both beam angle and spot size measurements since the DF iris diameter and the DF stop diameter are both set to 2 mm. The axial beam profile, however, measures the angle of light from the focus to below $(21 \pm 1)^\circ$ (0.35 NA). This is likely caused by observation error due to the low intensities at high angles. After confocally filtering the depth of focus, as measured on the CCD beam profile, is on average $4 \mu\text{m}$ across the supercontinuum wavelength range (Figure 1.6d).

Figure 1.7 shows the individual wavelength components that make up the integrated spectral signal in Figure 1.6d. As expected the depth of focus increases with wavelength. The

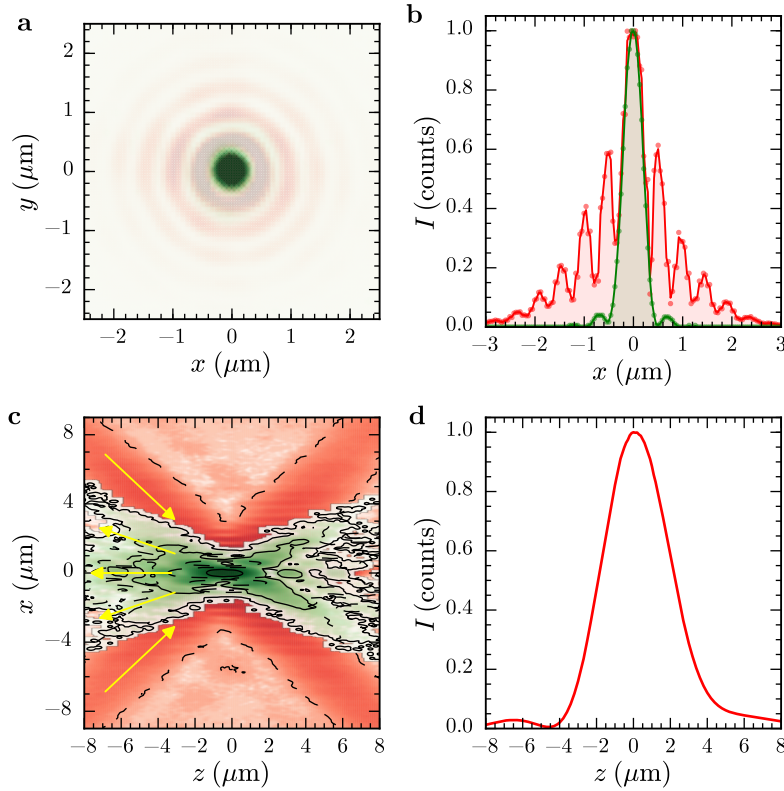


Figure 1.6: Beam profiling of dark-field filtered supercontinuum illumination (red) and scattering collection (green) beam lines. Supercontinuum laser light is reflected back from a Ag mirror in the objective focus to characterise the illumination pathway. The spectroscopy pathway is characterised by coupling a 532 nm laser into a single mode fibre and passing it through the collection optics with the DF-iris closed to 2 mm. The stated axial distance z is twice the displacement of the mirror to account for reflections to the focal plane. Lateral distances are calculated using the CCD array size and pixel dimensions. (a) Lateral beam profile of the illumination and collection focusses as measured on the CCD. (b) Intensity cross sections through the lateral beam profiles of the illumination and collection. (c) Axial cross section through the focus of illumination and collection beams. (d) Normalised summation of spectrometer counts of confocally localised supercontinuum light passing through the collection optics.

depth varies from (2.8 ± 0.1) μm at $\lambda = 500$ nm to (6.4 ± 0.1) μm at $\lambda = 1100$ nm. The chromatic structure of the beam is non-linear and shows that the colour maxima for $\lambda < 550$ nm and $\lambda > 800$ nm occur slightly offset from the pinhole position. Overall this does not detract much from the measured spectra since intensity differences in the chosen focal plane are normalised with the reference spectrum.

Lateral localisation is more important to consider than axial sectioning. Scattered light from a sub-wavelength size nanoparticle provides a point source from which the PSF can be measured across a small, resonant bandwidth. By (raster-) scanning a strongly-scattering metallic nanoparticle (MNP) under the beam its point scattering response is convoluted with the beam structure in the focus. The size of the confocal pinhole determines how much of this beam structure is laterally filtered prior to spectroscopy and thus, by measuring the scattering

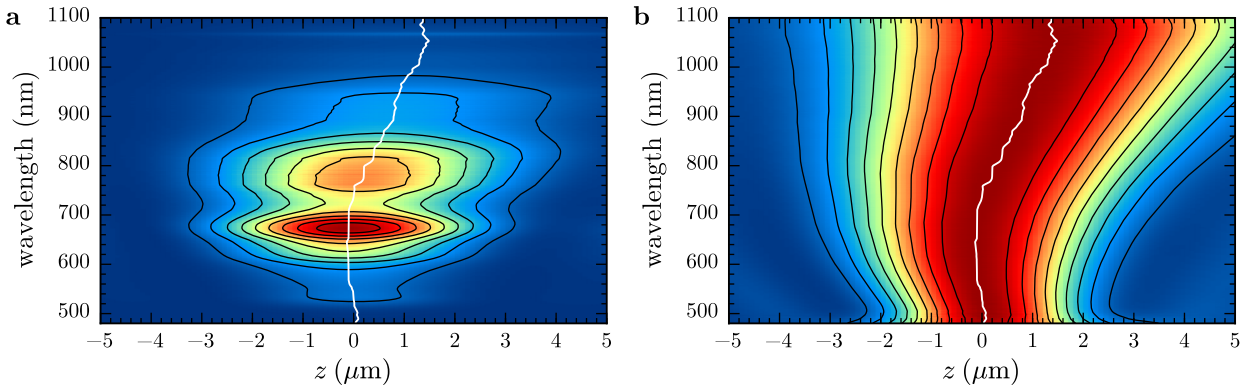


Figure 1.7: Axial chromatic aberration at each wavelength through the objective focus. The image is formed from spectra of the *s*-polarised component of a reflection from a Ag mirror scanned through the focus. An intensity plot normalised for each wavelength is shown to determine depth of focus. The white indicates the position of maximum signal along the optical axis for each wavelength and shows the distinctive bowing curve of chromatic aberration.

spectra, the actual PSF, as seen by the spectrometers, can be mapped across a broad range of wavelengths. It is this function that determines the specific locations from which spectra are collected and becomes particularly important when attempting to measure localised scattering from an extended nanostructure.

Figure 1.8 shows scattering profiles extracted from AuNP scans, demonstrating the effective spectral PSF for a range of pinhole diameters. 80 nm AuNPs on glass resonantly scatter at 550 nm due to excitation of the dipolar localised surface plasmon (LSP). A single AuNP was chosen on which multiple scans were performed, changing and realigning the confocal pinhole in between each scan. Wavelength slices at the AuNP surface plasmon resonance (SPR) (Figure 1.8a–c) show the lateral effective PSF. Without a pinhole in place the spectral PSF is a convolution of the focal beam profile shown in Figure 1.6a. The spectrometer sees the scattering from all the concentric rings in the focus so localisation of spectral features to the beam centre cannot be guaranteed. Decreasing the pinhole diameter filters scattering from the focus and removes the contributions to spectra from the outer rings until spectra can only be acquired from the central spot. This guarantees localisation of observed spectral features to a finite-sized region. The FWHM of the scattering signals on resonance are (255 ± 25) nm with the 25 μm pinhole in place, (260 ± 25) nm with the 50 μm pinhole in place, and (300 ± 25) nm without a pinhole. The FWHM at 900 nm for the case of the 25 μm pinhole is 410 nm for reference. Due to the single AuNP being the only source of scattering in each of the scans the measured spectrum is the same for all pinholes (Figure 1.8e). Though the resolution is not improved by a great amount, use of the smaller pinhole does guarantee better spectral localisation, as seen by the presence of only the central maximum in its PSF.

Fitting the centroid at every wavelength in the spectral data cube identifies lateral chromatic aberration in the microscope. This is an important parameter to consider when using

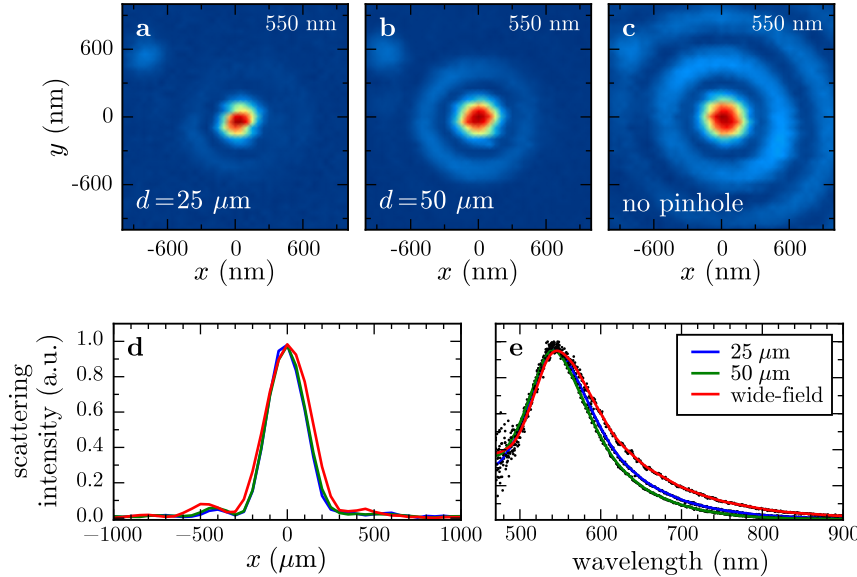


Figure 1.8: Hyperspectral scans of AuNPs used to characterise the lateral PSF with different confocal pinhole diameters. (a-c) Wavelength slices of AuNP scans on resonance using 25 μm and 50 μm diameter pinholes and finally no pinhole, respectively. (d) The extracted PSF from line profiles across the images (a-c). (e) Spectra of AuNPs imaged. Localisation is observed with reduced pinhole diameter as the concentric illumination rings are cut.

hyperspectral imaging or when acquiring spectra. For example, if the chromatic aberration is systematic and fitted then a correction offset can be added to hyperspectral data cubes at each wavelength. Spectra from each pixel can then be further recombined into regular RGB images by integrating the spectra at each pixel with RGB pixel spectra.

Figure 1.9 shows the centroids of the PSFs across the SPR band for each pinhole diameter. Scattering centroids are extracted from each wavelength slice using discrete image moment analysis,

$$M_{ij} = \sum_x \sum_y x^i y^j I(x, y), \quad (1.2)$$

where i, j denote the moments of the x, y axes.⁹ The position of maximum scattering is then given by,

$$(\bar{x}, \bar{y}) = \left(\frac{M_{10}}{M_{00}}, \frac{M_{01}}{M_{00}} \right). \quad (1.3)$$

Displacements are scaled relative to the centroid position on resonance where the signal is highest. The centroid position drifts almost linearly by 80 nm in the x -direction and 80 nm in the y -direction. Since the pinhole only filters the outer rings of the PSF there is very little

⁹Note that the discrete image moments are based on the continuous moment theorem with moments given by

$$M_{ij} = \int_{-\infty}^{\infty} \int_{-\infty}^{\infty} x^i y^j f(x, y) dx dy.$$

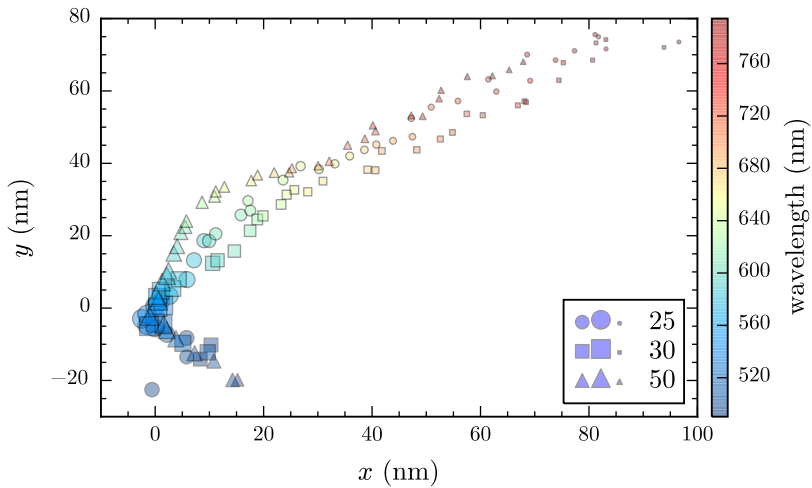


Figure 1.9: Measurements of lateral chromatic aberration across the plasmon resonance scattering bandwidth from hyperspectral images of AuNP. The central position of the scattering centroid is extracted from images at each wavelength. Changes in centroid position with wavelength signify chromatic aberration.

difference in the centroid positions between pinholes. As the range of centroid displacement in each direction is well below the diffraction limit and corresponds to only a few pixels offset in each image, the aberrations are not considered to negatively impact spectroscopy.

To summarise, a microscope platform has been designed to accommodate various sample geometries, specifically AFM tips. Single nanostructure spectroscopy is enabled by utilising an ultra-high brightness supercontinuum laser in a dark-field optical geometry, capable of measuring spectra between 500–1100 nm with short exposures, as low as 10 ms, allowing for time-efficient measurement of dynamic nanostructures. Beam profiling clearly shows that the supercontinuum dark-field technique works as expected and that spectra are collected from a small volume in the objective focus due to confocal localisation.

1.3 Electronics Design

By applying a voltage, V , and measuring the current, I , the conductance, G , of a conductive junction between tips can be determined using $I = GV$. Using this, quantum electronic transport can be measured and correlated with optical measurements to gain a sense of spatial separation and the extent of charge transfer across the gap.

The experimental chamber contains two triaxial connectors, one attached to each Cu tip clamp, to send and return electronic signals, permitting biasing and electrical measurement of the gap between AFM tips. Electronic signals are controlled and redirected using a control box, which attaches to the chamber triax cables. Electronics are split between an a.c. circuit that drives a resonant capacitive tip alignment procedure and a d.c. circuit for electrical

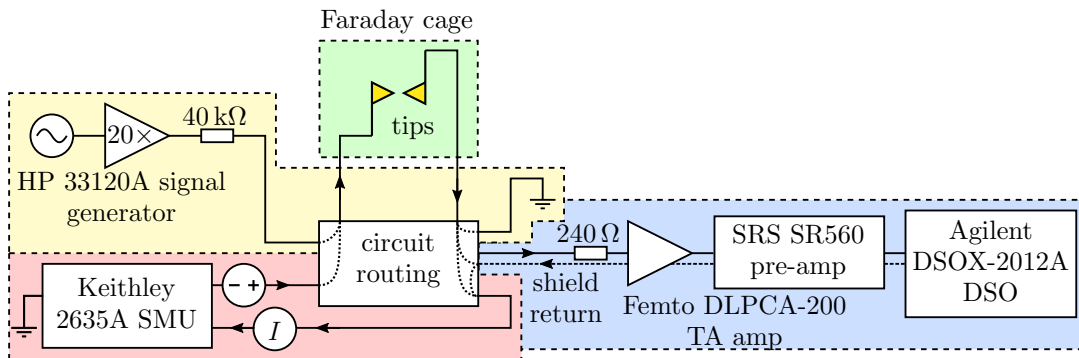


Figure 1.10: Block schematic of the electrical circuit design. The central routing box allows switching between a.c. and d.c. circuits and low-and high-bandwidth d.c. measurements. The a.c. circuit is used to align two AFM probes together while the d.c. circuit is used to measure spatially dependent signals from the gap between two AFM probes.

measurements. The d.c. electronics are further split into low and high bandwidth measurement circuits. The low bandwidth ($< 10 \text{ Hz}$) circuit measures electronics continually over long time periods, typically giving spatial information linked to sample separation. The high bandwidth circuit operates on a trigger to capture single shot events on much shorter time scales. Both d.c. circuits are typically run simultaneously while the a.c. and d.c. circuitry is manually switchable. A block schematic of this system is shown in Figure 1.10.

The a.c. circuit consists of a signal generator connected to a $20\times$ voltage amplifier to drive the junction capacitance. This is used to resonantly drive an AFM cantilever into oscillation and align tips into a tip-to-tip dimer configuration. A $40 \text{ k}\Omega$ current limiting resistor is placed after the amplifier to prevent damage to the tip junction in the event of a direct conductive contact.¹⁰ The return signal from the circuit is then terminated at ground. The separate d.c. circuit consists of a source-meter unit (SMU) circuit for low-bandwidth (sub- 10 Hz) measurements with a switchable high-bandwidth measurement extension. The SMU (Keithley 2635A) is used to apply a voltage across the junction and measure the current. The switchable high-bandwidth path routes the current through a $10^4\times$ gain transimpedance amplifier (Femto DLPCA-200) followed by a 1 MHz low-pass filtering stage (SRS SR560). The amplified voltage is measured on a digital storage oscilloscope (DSO) (Agilent DSOX-2012) with the shield becoming the return path of the current back to the SMU via the routing box.¹¹

The fundamental feature of the combined circuitry is their separability. The a.c. circuit is not required to be low-noise but the d.c. circuitry is used to measure low-level tunnelling currents. For the d.c. circuit to operate correctly it must be isolated from all other electronics.

¹⁰The optimum resistance value is calculated using $R = V/I_{\text{limit}}$ where $V = 10 \text{ V}$ typically and a safe current limit is $I_{\text{limit}} = 250 \mu\text{A}$. This gives a resistance of $40 \text{ k}\Omega$.

¹¹An alternative strategy for converting a current into a voltage is to pass the current through a well-known resistor and differentially amplify the voltage drop across the resistor. This was not used since the transimpedance amplifier was readily available and of a low noise specification.

The a.c. circuit remains completely disconnected and held at ground when the d.c. circuit is engaged, and vice-versa. To achieve measurements of small, sensitive currents, reducing the noise level to a minimum is imperative. The noise floor at low bandwidths, along with the current range of the SMU, sets the minimum current which can be measured. The sub-10 Hz bandwidth of the SMU removes much of the noise during spatial measurements. Correct grounding of all electronic chassises to a single point (the SMU) shields EMI and prevents ground loops from inducing current offsets. Triax cabling is used with guarded connections where possible to prevent leakage currents.

A standard operating voltage between 10–50 mV is used to drive high quality tunnelling currents. Conductances greater than $10^{-8}G_0$ are then clearly measured above noise. Using lower voltages means currents are only observable for larger tunnelling conductances, i.e. smaller gap widths, whilst higher voltages lead to larger overall currents and electrostatic interaction between tips, both of which should be avoided to prevent damage to the tip junction. To maintain good scan speeds the current range is restricted to 10 nA with a ± 10 pA error, since more accurate ranges have longer settling times. Limiting the current range is the dominant source of current measurement error as opposed to the noise floor.

Noise on the SMU is measured by varying a series resistance in place of the tip junction and taking the standard deviation of 20 measurements across a range of voltages in 10 mV steps. The open circuit noise measures ± 10 pA. Johnson noise for such a circuit is estimated to be around 1 pA. If current measurements are strictly limited by the current range then the percentage error of each range should be equivalent. This is not the case, with the percentage error increasing from $10^{-3}\%$ to $10^{-2}\%$ as the current decreases to the nA range, signifying the approach of the noise floor. Actual noise levels around ± 100 pA are found at 50 mV with a $1\text{ M}\Omega$ ($10^{-2}G_0$) junction resistance characteristic of electron tunnelling in the quantum regime of plasmonics. Given the small percentage errors, circuit noise is not a problem for tunnelling current measurements.

Noise predominantly affects high bandwidth measurements, where it limits the conductance resolution and minimum trigger level for single shot measurements. High bandwidth noise typically originates from digital circuitry, e.g. switch-mode power supplies and powered relays. Power supplies are therefore covered in foil to shield EMI and manual toggle switches are used instead of remote-controlled relays. Applying a 1 MHz filter goes some way to reducing high bandwidth noise. Any more filtering smooths measurements too much.

The maximum allowed current is set to 250 μ A to prevent damage to contacted AFM tips. Upon surpassing this limit the SMU attenuates the voltage to reduce the current. A current limiting resistor is also included in the circuit to ensure a hardwired maximum and to prevent overloading of the DSO and transimpedance amplifier. The value of this resistor is calculated

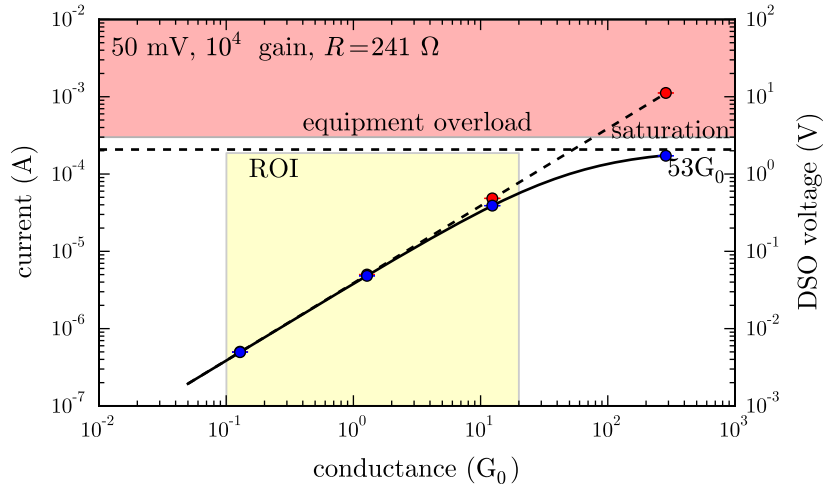


Figure 1.11: Characterisation of electronic measurements based on junction conductance. Solid lines show the calculated SMU currents and amplified voltages for given junction conductances under a 50 mV applied voltage with a 241 Ω current limiting resistor to prevent saturation (high bandwidth circuit). Dashed lines show the calculated oscilloscope voltages for the case without the current limiting resistor (low bandwidth circuit). Circles mark experimentally measured points using resistors in place of the junction in both circuits. Error bars are present but too small to visibly see.

using,

$$R = \frac{AV}{0.95V_{\text{overload}}}, \quad (1.4)$$

where V is the operating voltage, A is the amplifier gain and V_{overload} is the minimum overload voltage for the circuit at a given voltage V (determined by whichever overload voltage is surpassed first, either the maximum transimpedance input current of 5 mA pre-amplification or the maximum output voltage of 5 V). The pre-factor of 0.95 is chosen to prevent the current getting close to overloading. For a 50 mV bias and 10⁴ gain the ideal resistance is 175 Ω but for a 10 mV bias with 10⁵ gain it increases to 350 Ω . To accommodate a range of voltages and both gain settings, a middle resistance of 241 Ω is used, which provides some headroom for increasing the voltage at the lower gain. The calculated current and DSO voltage as a function of junction conductance for the low and high bandwidth circuits is shown in Figure 1.11. Excellent agreement with experimental current and voltage measurements taken with a set of resistors demonstrates the circuit behaves exactly as predicted.

The presence of the current limiting resistor means that measured circuit conductances, G_{measured} , contain a series resistance that needs to be taken into account. Junction conductances are calculated using,

$$G_{\text{junction}} = (G_{\text{measured}}^{-1} - R)^{-1}. \quad (1.5)$$

The maximum conductance value that can be measured is found by inverting the limiting

resistance using $G_{\max} = 1/R$. For a 50 mV bias the conductance limit is $53G_0$. Conductances greater than this value are small compared to the series resistance and are therefore much harder to measure reliably. For this reason the range of interesting conductances ($G < 20G_0$) is ideally kept to the linear part of the current curve by limiting the voltage and gain.

1.4 AFM Design: Measurements of Force

An AFM module measures cantilever deflections as they flex under an applied force. The linear displacement of the cantilever, Δz , from its equilibrium position under an applied force, F , is simply given by,

$$F = k\Delta z, \quad (1.6)$$

where k is the stiffness or spring constant of the cantilever. Contact and tapping mode cantilevers are mostly used in experiments, for which $k = 0.2 \text{ N m}^{-1}$ and 40 N m^{-1} , respectively. The change in angle caused by a linear displacement at the tip can be measured optically as a change in deflection angle of a laser focussed on the back of a reflective cantilever (Figure 1.12). The sensitivity of this technique has led to it being named atomic force microscopy since atomic-scale forces cause measurable deflections, enabling topological imaging with nanoscale resolution. For tip-tip dimers, nano-scale force measurements become important as they dictate how tips come together and move through interfacial layers prior to electrical contact. A compact AFM module was thus constructed to monitor the tip-tip interaction forces during tip dimer measurements.

The AFM module consists of a compact optomechanical module, mechanically bolted onto the top plate of the microscope platform, and a separate 633 nm laser diode coupled together using a strain-relieved single mode fibre, as shown in Figure 1.13. Single mode fibre is used to produce a stabilised laser output. Light is focussed through an entry window in the experimental chamber onto the cantilever of a back-facing AFM probe during an experiment. The beam position is laterally offset on the focussing lens using a silver turning prism to focus on the cantilever at an angle so that reflections return through the AFM with the opposite lateral offset.¹² Light reflected back off the cantilever at a different angle in the focal plane is laterally translated in Fourier space. This translation is measured using a fast

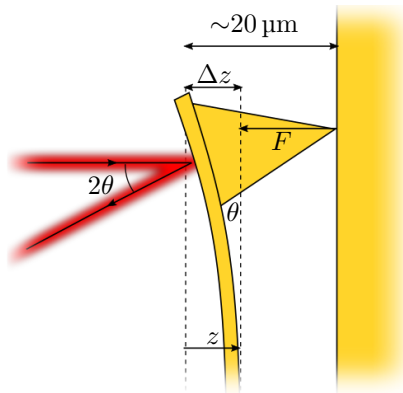


Figure 1.12: Concept of contact mode AFM. An applied force F bends the cantilever proportional to a linear displacement x . Light incident on the bent cantilever deflects at an angle 2θ .

¹²An alternative to this approach allows use of a common beam path but requires two polarisers and a quarter wave plate, leading to simpler alignment but a more costly design.

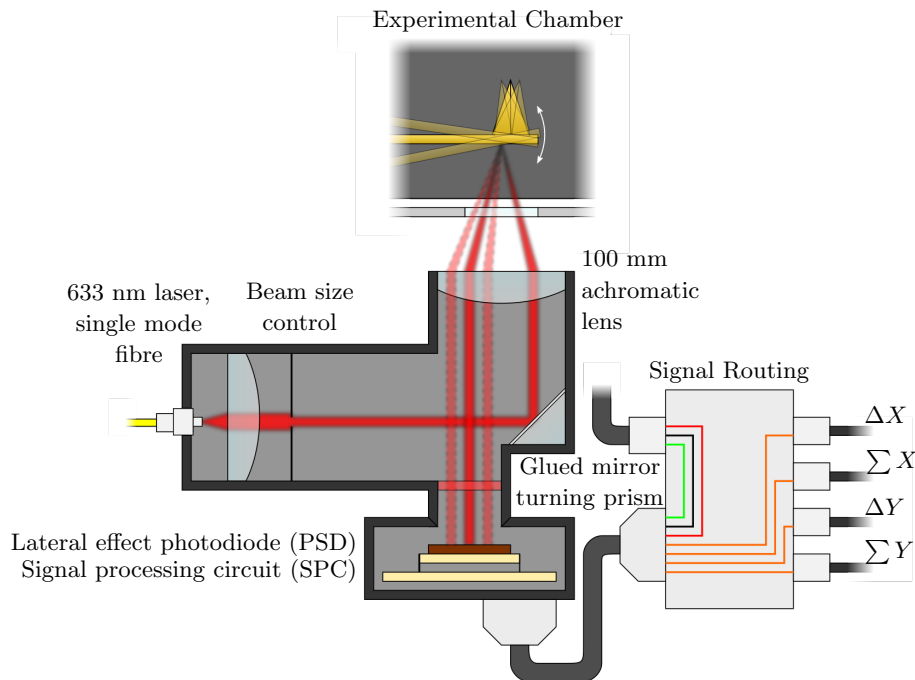


Figure 1.13: Schematic diagram of the AFM module attached to the side of the microscope platform. Incident light from a single mode fibre is focussed at an angle onto an AFM cantilever. Angled reflections from the cantilever are re-collimated into a laterally displaced beam whose position is detected on the PSD.

lateral effect photodiode, also known as a position sensitive detector (PSD), where the beam position generates a current in each orthogonal direction. The PSD contains a signal processing circuit with a built-in transimpedance amplifier (10^5 gain) to convert these small currents into voltages corresponding to the measurements $\Delta x, y$ and $\sum x, y$. Voltages are recorded using a DAQ card (NI X-series).

Changes in the voltage output of the PSD correspond directly to motion of the tip and cantilever under an applied force. The position of the PSD is adjusted with zero force applied to the cantilever to zero the voltage. The lateral displacement of the returning beam is then calculated using,

$$ds_i = \frac{L_i}{2} \frac{\Delta V_i}{\sum V_i}, \quad (1.7)$$

where i is the lateral axis, either x or y , L_i is the length of the detector along that axis (10 mm) and V_i is the voltage output at each end of the detector axis. The displacement can then be transformed into an applied force via a calibrated conversion.

The width of the cantilever and the radius of the input beam determines the minimum beam size. Cantilevers have a width of 50 μm therefore the spot size in the focus must be less than this value. Since the input is a single mode Gaussian beam the spot diameter, $2w_0$, is

given by $2w_0 = 4\lambda f/\pi D$, where f is the focal length and D is the collimated beam diameter. For $\lambda = 633\text{ nm}$ and a required spot size $2w_0 < 50\text{ }\mu\text{m}$ the fraction $f/D < 62$. The focal length is restricted by the distance from the edge of the top plate, where the AFM module is mounted, to the cantilever through the chamber window. A 100 mm lens is chosen to accommodate the focal length constraint, which restricts the beam diameter to $D > 1.6\text{ mm}$. This beam diameter is set by using a short focal length lens to collimate the single mode fibre output.

1.4.1 Calibrating the AFM

The displacement of the tip under an applied force is related to the lateral translation of the beam on the PSD. By determining the tip displacement, the force applied to the AFM tip can be measured using Eq. 1.6. The transformation from tip displacement into a measured lateral displacement in Fourier space is linear in the current geometry and can be expressed as,

$$s = k_{x \rightarrow s} x, \quad (1.8)$$

where $k_{x \rightarrow s}$ is the transformation constant. Each of the individual linear geometrical transformations required to convert the tip displacement into a measurable beam displacement in Fourier space (tip displacement to angular cantilever deflection to angular beam reflection to lateral translation on recollimation) are incorporated into this single constant, $k_{x \rightarrow s}$, which can be experimentally determined.

The simplest method of calibration involves pushing an AFM tip against a hard contact so that the displacement is known ($\Delta z = z$). From there the beam translation is measured as a function of tip displacement and data can be fitted to determine $k_{x \rightarrow s}$. The force can then be estimated using Eq. 1.6. Whilst this is not ideal as the cantilever spring constant is still somewhat unknown, the method is simple. Therefore, for force measurements, the value of the cantilever spring constant is assumed from the AFM probe data sheet. The large tolerances on stiffness measurements mean that this approach is only sufficient to estimate the applied force on a nano-gap to within 50%.¹³ Other methods of accurately measuring the cantilever spring constant do exist, as do methods to directly map the force to a measured signal, i.e. $F = k_{s \rightarrow F} s$, but add further complexity to experiments [8–16]. Since exact measurements of force are not crucial to current nano-gap studies, the uncertainty is acceptable.

¹³The fractional uncertainty is given by $\delta F/F = \sqrt{(\delta k/k)^2 + (\delta z/z)^2}$ for which $\delta z/z$ is negligible compared with $\delta k/k = \sim 0.5$.

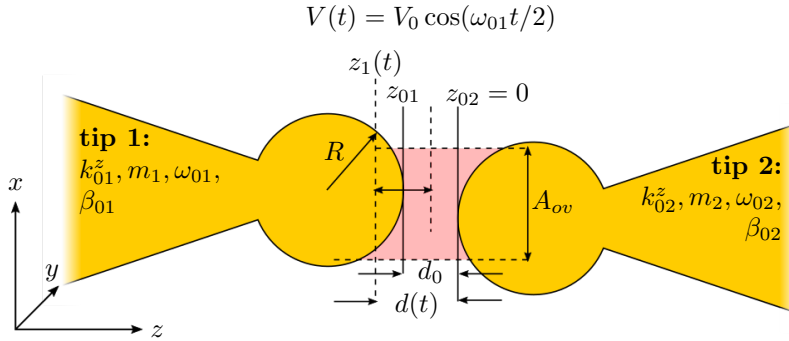


Figure 1.14: Diagram of tip alignment parameters. The position of one tip relative to the other is detected using a resonant scanning capacitance AFM technique. The gap is biased with an oscillating voltage to induce a resonant vibration of one of the AFM cantilevers. The amplitude of oscillation is sensitive to the gap size d and the area of overlap A_{ov} between tip features of characteristic size R . For sharp tips R is the apex radius whereas for nanostructured tips R is considered to be the feature size.

1.5 Scanning Capacitive AFM Tip Alignment

A significant challenge when attempting to recreate a plasmonic dimer using opposing AFM probes is the alignment of tips with the focussed laser spot in a symmetric tip-to-tip configuration. This capability is necessary to permit the majority of dual tip experiments and forms the first step to measuring the dynamical physical response of plasmonic tip dimer systems. For successful experiments the tolerance on the tip-to-tip alignment is less than $\mathcal{O}(R_{\text{tip}})$. Aligning tips using CCD imaging is limited by diffraction and therefore unsuitable. Initially this problem was solved using a non-linear capacitive alignment technique that required locking into the third harmonic of the driving signal [17]. Whilst functional in simpler systems, the technique was limited in its accuracy by the small pA level currents in the third harmonic mode and the extensive filtering and lock-in techniques required to measure these. A simpler approach is to simply use the AFM module optics to measure the oscillating cantilever deflection. This is more widely known as scanning capacitance mode AFM (SC-AFM) or scanning capacitance microscopy (SCM), and has been used in the past to measure the dopant levels in semiconducting substrates [18–22]. By utilising optical detection over direct electronic measurements tip alignment becomes segregated from the microscope electronic d.c. measurement circuitry and issues are no longer caused by noise leaking into the a.c. electronics.

1.5.1 Mechanism for Alignment of Two Opposing Tips

To a first approximation the metallic tips can be ignored and only the capacitive interaction between planar cantilevers is considered. Cantilevers are separated by a distance $d(t) = z_1(t) - z_2(t)$ and coupled via the z -components of the long range, attractive, electrostatic driving force F_{EL}^z and short range Van der Waals and repulsive tip-tip interaction forces F_{TT}^z .

Each cantilever has an associated spring constant k_{0i}^z , mass m_i and resonant frequency of oscillation $\omega_{0i} = \sqrt{k_{0i}/m_i}$. When vibrated, cantilevers oscillate around an equilibrium position z_{0i} . The equilibrium separation between tips is then denoted by $d_0 = z_{01} - z_{02}$.

The equation describing motion in the z -axis of the two parallel cantilevers, denoted by $i = 1, 2$, of spring constant $k_i^z = k_{0i}^z + k_{TT}^z$, coefficient of damping $\beta_i^z = \beta_{0i}^z + \beta_{TT}^z$ and mass m_i , is given by,

$$m_i \frac{d^2 z_i}{dt^2} + \beta_i^z \frac{dz_i}{dt} + k_i^z (z_i - z_{0i}) = \pm (F_{EL}^z + F_{TT}^z), \quad (1.9)$$

where the sign of the force is positive for one tip and negative for the other. Assuming that alignment takes place at long range, tip-tip interactions can be ignored, therefore $F_{TT}^z = 0$ and $\beta_{TT}^z = k_{TT}^z = 0$. The system is further simplified by assuming that one cantilever remains stationary by being stiff (tapping mode tip with $k \approx 40 \text{ N m}^{-1}$)¹⁴ and always being off resonance ($\omega_{01} \neq \omega_{02}$). This is usually satisfied in experiments where a stiff cantilever is required such that the optical probe is incident on the same sample area whilst under force. The apex separation is then restricted to $d = z_1$ with an equilibrium separation $d_0 = z_{01}$. Under these conditions the motion reduces to that of a single tip,

$$m_1 \frac{d^2 z_1}{dt^2} + \beta_1^z \frac{dz_1}{dt} + k_1^z (z_1 - d_0) = F_{EL}^z(z_1, t). \quad (1.10)$$

This equation now describes the whole system rather than each individual tip with the main reference point between tips being the equilibrium separation d_0 .

The remaining capacitive driving force exerted between tips is purely electrostatic and of the form,

$$F_{EL}^z(V, z) = \frac{1}{2} \frac{\partial C(z)}{\partial z} V^2(t), \quad (1.11)$$

where $C(z)$ is the capacitance between the tips at a distance z and $V(t)$ is the potential difference between tips. Under a parallel plate capacitor model the capacitance is $C(z) = (\epsilon_0 A_{ov}/z) + C_{bk}$ for plates with A_{ov} area of overlap at a separation z , including a stray capacitance C_{bk} . Applying a harmonic driving force at a frequency ω_s , described by $V(t) = V_0 \cos(\omega_s t)$, results in a nonlinear driving force, given by,

$$F_{EL}^z(z_1, t) = \left(\frac{-\epsilon_0 A_{ov} V_0^2}{4z_1^2} \right) [1 + \cos(\omega_p t)], \quad (1.12)$$

where $\omega_p = 2\omega_s$ is the cantilever pump frequency. Substituting Eq. 1.12 into Eq. 1.10 gives the simplified equation of motion for the dual-tip system,

$$m_1 \frac{d^2 z_1}{dt^2} + \beta_{01}^z \frac{dz_1}{dt} + k_{01}^z (z_1 - d_0) = \left(\frac{-\epsilon_0 A_{ov} V_0^2}{4z_1^2} \right) [1 + \cos(\omega_p t)]. \quad (1.13)$$

¹⁴This is based on data sheet values of almost all tapping mode tips.

Driving at a pump frequency close to the cantilever resonance ($\omega_p \approx \omega_{01}$) leads to a resonant oscillation between tips. For small oscillations around d_0 , Eq. 1.13 can be Taylor expanded to first order into the form of the damped Mathieu equation¹⁵ with an approximate solution¹⁶

$$z_1 \approx d_0 - |z_1^{off}| - z_{m1} \cos(\omega_p t + \varphi_1) \quad (1.14)$$

where

$$z_1^{off} \approx \frac{\varepsilon_0 A_{ov} V_0^2}{4d_0^2 \langle k_{e1}^z \rangle}, \quad (1.15a)$$

$$z_{m1} \approx \frac{\varepsilon_0 A_{ov} V_0^2}{4d_0^2 \sqrt{(\langle k_{e1}^z \rangle - m_1 \omega_p^2)^2 + (\beta_{01}^z \omega_p)^2}}, \quad (1.15b)$$

$$\varphi_1 \approx \tan^{-1} \left(\frac{\beta_{01}^z \omega_p}{\langle k_{e1}^z \rangle - m_1 \omega_p^2} \right), \quad (1.15c)$$

in which $\langle k_{e1}^z \rangle$ is the effective spring constant of the system, $\langle k_{e1}^z \rangle = k_{01}^z - \varepsilon_0 A_{ov} V_0^2 / 2d_0^3$, taking into account the time-averaged electrostatic interaction. From Eq. 1.15b and Eq. 1.15c it can be seen that both the oscillation amplitude and phase relative to the driving signal vary with the equilibrium separation d_0 .

Although the model is for two parallel plates, it becomes applicable to tips in a dimer configuration once the separation is sufficiently low that the tip-to-tip capacitance dominates over all other capacitive contributions (such as the cantilever or tip facet interactions). In this regime, if the tips stray out of alignment the tip-to-tip distance increases and the capacitance decreases, reducing the tip oscillation amplitude and the phase, hence tips are aligned when both the amplitude and phase are maximised. Both these properties are readily measurable using optical cantilever deflection in the AFM module.

Whilst optical detection gives a better signal-to-noise and measures at higher bandwidths, it should be noted that the capacitive model was originally developed to show that a $3\omega_s$ current signal can be used to align tips [17]. By driving the system with $\omega_p \approx \omega_{01}$, a mechanical parametric resonance is excited at $2\omega_{01}$ (otherwise only the fundamental is excited with resonant driving) and the current through the tip junction is given by,

$$I(\omega_s) \approx \omega_s C_0 V_0 \left(1 + \frac{|z_{off}|}{d_0} + \frac{z_{m1}}{2d_0} e^{i\varphi_1} + \frac{C_{bk}}{C_0} \right) e^{i\frac{\pi}{2}}, \quad (1.16a)$$

$$I(\omega_p + \omega_s) \approx \frac{(\omega_p + \omega_s) C_0 V_0 z_{m1}}{2d_0} e^{i(\varphi_1 + \frac{\pi}{2})}, \quad (1.16b)$$

where $C_0 = \varepsilon_0 A_{ov} / d_0$ and z_{off} is an additional offset due to $F_{EL}^z \propto V^2$. Non-linear oscillations

¹⁵Damped Mathieu equation: $\ddot{z} + 2\kappa\dot{z} + [a - 2q \cos(2t)]z = 0$

¹⁶Full derivation available in the appendix.

in the tip capacitance result in parametric frequency mixing in the electronics with resulting signals at the sum and difference frequencies, $\omega_p + \omega_s = 3\omega_s$ and $\omega_p - \omega_s = \omega_s$ respectively. The signal at $3\omega_s$ is background-free, as shown in Eq. 1.16b, and once again depends only on z_{m1} and d_0 . However, currents are $\mathcal{O}(\text{pA})$ for acceptable driving voltages, therefore alignment only works over shorter ranges, and requires larger voltages to further boost the oscillation amplitude and low-noise detection electronics. Optical detection is advantageous as small oscillations at lower voltages are easily detectable, which protects the samples from damage caused by tapping between tips once the gap is small.

1.5.2 Numerical Modelling and Experimental Measurements of Scanning Capacitance Tip Alignment

Numerical Modelling of Tip Alignment

Theoretical curves for the system response based on Eq. 1.13 for a typically used contact/tapping mode AFM probe dimer are solved numerically using an ordinary differential equation (ODE) solver.¹⁷ Results are intended to *qualitatively* demonstrate the alignment technique. The following table summarises the parameters of the model for each tip:

	Tip 1	Tip 2
k_0 (N/m)	0.2	40
ω_0 (kHz)	$2\pi.13$	$2\pi.300$
$\Delta\omega$ (Hz)	$2\pi.200$	$2\pi.200$
r (nm)	20	20

Table 1.1: Tip parameters used in numerical calculations. The dimer is assumed to comprise of a dynamic contact mode AFM cantilever (tip 1) and a fixed tapping mode cantilever (tip 2).

The plate area is assumed to be πr^2 where r is the radius of the tip. This is estimated to be $r = 20\text{ nm}$ based upon standard tip apex dimensions. Changing this value does not change the overall qualitative shape of the data. The mass of each tip is calculated from the resonance using $m_i = k_{0i}/\omega_{0i}^2$. The damping coefficient of each tip is given by $\beta_{0i} = 2m_i\delta_i$ where $\delta_i = \omega_{0i}/2Q_i$ and $Q_i = \omega_{0i}/\Delta\omega$ (a quantity which is verifiable by experiment). Only the damping coefficient of the vibrating tip matters at any given time due to the large difference in resonant frequencies. To maximise the detected response the system is studied around the resonance of the soft cantilever. The system spring constant is given by,

$$k_0 = (k_{01}^{-1} + k_{02}^{-1})^{-1}, \quad (1.17)$$

¹⁷ODE in Numpy/Python

and the system mass is given similarly by,

$$m = (m_1^{-1} + m_2^{-1})^{-1}. \quad (1.18)$$

The forces acting on the tip are described by a capacitive driving force, described by Eq. 1.12, and an interaction force. The interaction force is described by,

$$F_i^z(z) = \begin{cases} -\frac{Hr_1}{6(a+z_c)^2}, & \text{if } z_c + a > a_0 \\ -\frac{Hr_1}{6a_0^2} + \frac{4E\sqrt{r_1}}{3-3v^2}(a_0 - a - z_c)^{\frac{3}{2}}, & \text{otherwise} \end{cases} \quad (1.19)$$

where z_c is the equilibrium position, a is the amplitude of the oscillation, a_0 is the equilibrium separation and H is the Hamaker constant [23–26]. The capacitive driving force depends only on the time-averaged tip separation whilst the interaction force depends on the oscillation amplitude of the tip around its equilibrium position compared with the gap separation since this eventually leads to tapping on the opposite tip.

The ODE algorithm computes the change in the cantilever position and velocity in time using their respective differentials,

$$\dot{z}_+ = \dot{z}_-, \quad (1.20)$$

$$\ddot{z}_+ = -m^{-1} [\beta_1^z \dot{z}_- - k_0^z z_- + F_{EL}^z(t) + F_i^z(z_-)], \quad (1.21)$$

where $F_{EL}^z(t)$ is the capacitive driving force described in Eq. 1.12, $F_i^z(z)$ is the interaction described in Eq. 1.19. The tip motion in time is solved, subject to stationary initial conditions, for 100 AFM oscillation periods. The steady state harmonic properties of the waveform are extracted using a sinusoidal fit to the last 50 periods, when behaviour has stabilised.

The modelled frequency response is determined by driving a spatially fixed tip dimer, separated by 100 nm, with a 10 V driving signal across a range of frequencies around $\omega_s = \omega_{01}/2 = 2\pi.13 \text{ kHz}/2$. The intertip separation is then varied while driving on resonance at various voltages to find the separation response.

Experimental Measurements using Scanning Capacitance Microscopy

Experimental measurements of capacitive tapping mode tip interaction use the AFM optics on the microscope and monitor the position of the tip through the motion of the reflected laser beam. The backside of the softer cantilever of the pair is illuminated by the 633 nm laser beam. By resonantly driving an AFM tip electronically its oscillation generates a signal $A \cos(\omega_p t + \phi)$ along one of the axes on the PSD. Lock-in detection is used in the software to remove noise and add phase sensitivity to signal measurements by referencing the oscillation to the driving

signal. The NIDAQ device simultaneously acquires both PSD signals in each direction along with the driving signal from the function generator output. The second harmonic of the driving frequency, ω_p is locked-in using the reference periodicity. The phase difference ϕ is then measured relative to the reference phase.

Experimental measurements are performed on a tip dimer consisting of a 13 kHz, 0.2 N m^{-1} soft Au contact-mode AFM cantilever and a 300 kHz, 40 N m^{-1} stationary Au tapping mode AFM cantilever. The resonance frequency of the softer cantilever is determined prior to tip alignment at long range by scanning the driving signal frequency and measuring the cantilever response. The separation response is probed by aligning the soft tip to the position of maximum amplitude by laterally scanning the xy plane opposite the stiff tip. The soft tip is approached towards the stationary tip along the z axis and the cantilever response is measured. The rate of approach varies between 0.5–2 nm per step depending on how far apart tips are separated. The amplitude is monitored in real time and the tip is retracted once the signatures of tapping are detected. Quick retraction is necessary as tapping with a soft cantilever is unstable to effects such as snap-in and short-range attractive forces. There is also a high chance of damaging the metallic tip coating during contact. Judgement of the retraction point is subjective since the point of snap-in cannot be predicted but preserves the tip for multiple cycles. This approach-reaction cycle is repeated many times with a continuously reducing voltage until tapping is difficult to achieve without the oscillation immediately becoming unstable. This occurs once driving with less than 5–6 V.

Comparison between Numerical Modelling and Experimental Scanning Measurements

Figure 1.15a shows the calculated frequency response for a dimer comprised of a stiff, tapping mode cantilever and a softer contact mode cantilever. From this the cantilever resonance can be clearly seen. The amplitude line shape matches the expected Lorentzian response of a damped resonator and oscillations transition between in-phase oscillation when driving at lower frequencies and anti-phase oscillation at higher frequencies. This is standard resonator behaviour as expected. The measured frequency response of a capacitively-driven contact mode AFM cantilever (Figure 1.15b) agrees well with the modelled response. The resonance frequency is higher than expected due to the tolerance range of real AFM cantilevers. One noticeable difference is the linear gradient superimposed onto the phase response. This stems from time lags during acquisition which give a linear phase offset with increasing frequency.

The calculated separation response for the same contact/tapping-mode tip dimer is shown in Figure 1.16a. As the separation decreases the capacitance between tips increases and resonant oscillation is amplified. This amplification occurs until the amplitude is equal to the separation, at which point the system transitions into the tapping mode of AFM imaging.

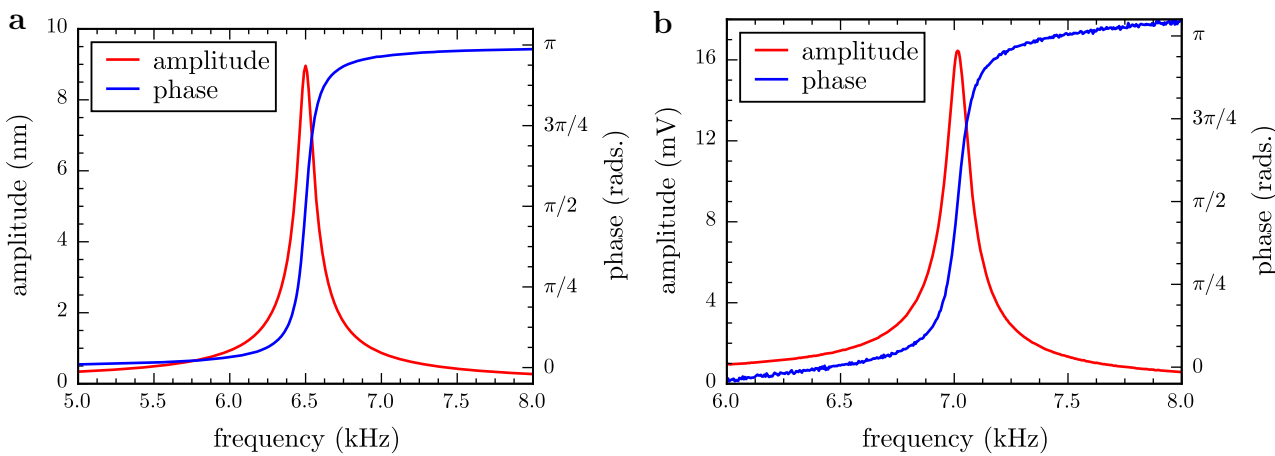


Figure 1.15: Theoretical and experimental frequency response showing the amplitude and phase of a standard opposing AFM tip system. The modelled tip junction (a) consists of a 13 kHz, 0.2 N m^{-1} soft tip and a 300 kHz, 40 N m^{-1} stationary tip, held at 10 V with a 100 nm intertip separation. Experimental cantilevers (b) are a 13 kHz, 0.2 N m^{-1} BudgetSensors ContGB Au tip and a 300 kHz, 40 N m^{-1} BudgetSensors TapGB Au tip, separated by $\sim 1 \mu\text{m}$ and driven at 15 V.

This is shown by the linear relationship of unity gradient between amplitude and separation, regardless of voltage. In this regime the oscillation is restricted by the gap width between tips, which limits the maximum possible amplitude. Calculations indicate that phase contrast only occurs once the oscillating tip comes into close proximity with the other tip. This onset of phase contrast occurs close to the point of maximum amplitude just before tapping. The phase is therefore a good indicator of the alignment between tips. Tips can be considered to be aligned once the centres of both the amplitude and phase overlap in a plane perpendicular to the two tips. The accuracy of these solutions becomes limited when the separation is reduced well into the tapping mode regime as the oscillation is difficult to sustain and surface (interfacial) forces begin to dominate, leading to the snap-in effect.¹⁸ This instability is seen by the deviation of the amplitude from its linear decrease in the tapping regime followed by its rapid decay.

Figure 1.16b shows the corresponding experimental curve to the numerically calculated separation response. The expected capacitive increase in amplitude followed by a linear tapping mode regime is qualitatively found in the experimental data. Differences from numerical calculations, such as the less drastic capacitive amplitude increase, are likely due to the large extended shape of the tip and cantilever not taken into account in the simple parallel plate model. The linear decrease is also less steep suggesting that only the upper region of the modelled curve is visible. The amplitude instabilities found in the calculations at small separations are also found in the experimental data. Repeat approaches after such an instability

¹⁸Snap-in, also known as snap-to-contact, is an AFM phenomenon described in a later chapter as a result of capillary forces from a water meniscus in the gap.

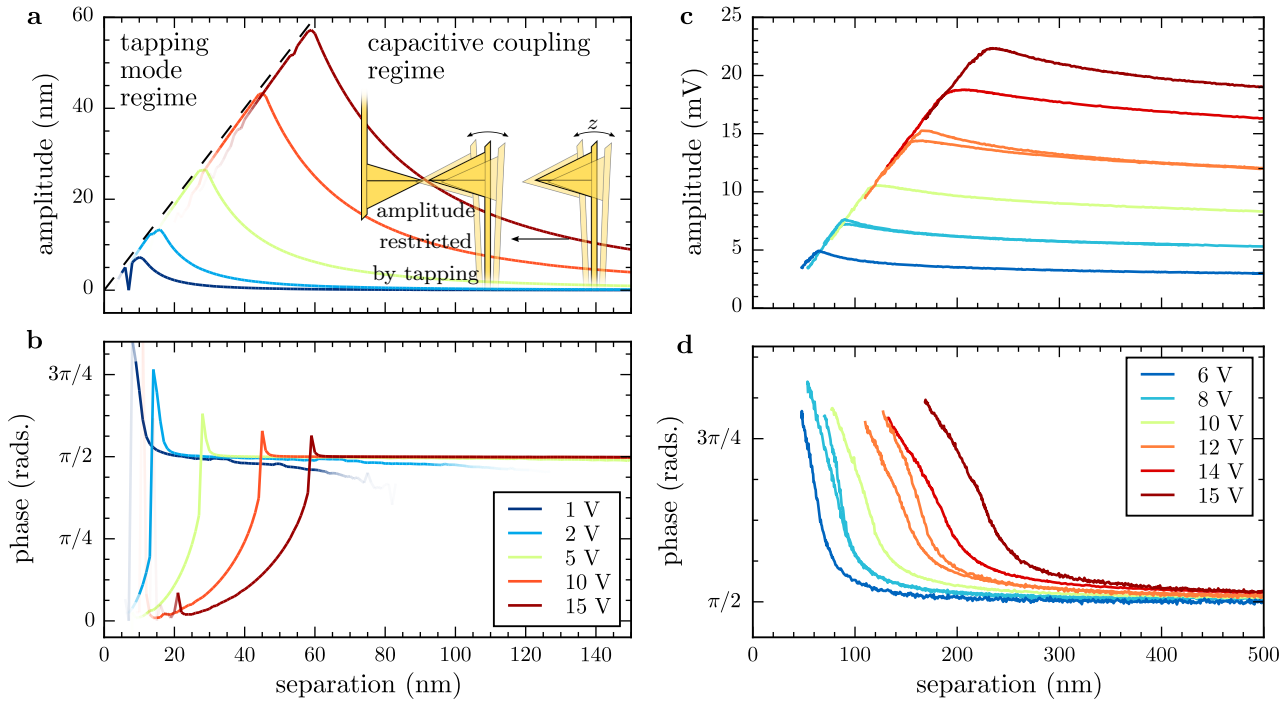


Figure 1.16: Theoretical and experimental separation response showing the amplitude and phase of a standard opposing AFM tip system. The modelled tip junction (a, b) consists of a 13 kHz, 0.2 N m^{-1} soft tip and a 300 kHz, 40 N m^{-1} stationary tip. The voltage across the modelled tip junction is varied while on resonance ($\omega_s = 2\pi \cdot 6.5 \text{ kHz}$). The amplitude increases as the intertip separation is reduced. The dashed line shows the point at which the oscillation amplitude is equal to the separation. For separations below this limit, the hard surface restricts the amplitude to the gap between tips. A diagram of this is shown as an inset. Experimental cantilevers (c, d) are a 13 kHz, 0.2 N m^{-1} BudgetSensors ContGB Au tip and a 300 kHz, 40 N m^{-1} BudgetSensors TapGB Au tip. The same vibrating tip is approached and retracted with the voltage reduced between each approach cycle. The amplitude increases as the intertip separation is reduced until oscillation becomes restricted by the gap width.

show different peak amplitudes with the differences attributed to misalignment after contact, changes in tip morphology or surface modification. Interestingly, the discontinuous reduction in the phase is not experimentally observed. This means that either the separation was not reduced enough for this to occur before retraction or the model is not completely correct. Both statements are equally likely due to the simplicity of the model used. Overall the cantilever behaviour qualitatively matches many of the trends predicted using a simple mathematical model solved using an ODE solver. As expected, the separation sensitivity of this technique makes it highly suited for tip alignment.

Another application for capacitive driving, demonstrated by Figure 1.16, is to use the long range interaction to lock the positions of the tips relative to each other, using the separation-dependent amplitude response as a feedback mechanism in a PID loop.¹⁹ Dynamic positioning

¹⁹Proportional-integral-differential (PID) control loops are a form of feedback mechanism for stabilising a value at a preset target.

and alignment between two tips can then be locked and maintained throughout an experiment to account for fluctuations due to either mechanical or thermal drift. Smaller separations can be locked by decreasing the voltage to reduce the amplitude up until the point at which the second harmonic signal becomes difficult to detect. The onset of tapping also limits the minimum achievable separation as the tip must remain oscillating. This technique could potentially become more useful if a stable plasmonic gap size is required for a long time whilst the contents or properties of the gap are modified.

1.5.3 Experimental Alignment of Tips using Scanning Capacitance AFM

By mapping the lateral amplitude and phase variations of the cantilever deflection on resonance, two opposing tips can be experimentally aligned. Alignment is carried out on resonance by laterally scanning the oscillating, soft cantilever tip over the stationary tip whilst reducing the separation. The location of the opposite tip is then determined by the position of maximum amplitude and phase. To prevent tip collisions due to entering the tapping regime, the voltage is reduced along with the separation. This allows only the minimum required signal for positional analysis. Unlike the phase, the amplitude signal varies smoothly over a longer range. As the intertip separation decreases, the amplitude centroid converges on the position of the opposing tip apex and the phase begins to increase and form a sharp peak. By iteratively following the lateral position of maximum amplitude the tips can be brought into alignment. This procedure is advantageous as it operates at long range in the non-contact regime, prior to the tapping mode regime.

Figure 1.17 shows a typical alignment scan at close range with peaks in both the amplitude and phase. At this point during the procedure the tips are considered to be well aligned. Tips are then brought into alignment by identifying the position of the peaks. Since the tips are only symmetric along one axis, long range capacitive coupling is inhomogeneous and skewed until the distance between tips is small enough that the tip-to-tip capacitance dominates interactions. Gaussian fitting is therefore potentially inaccurate in determining the peak location. Calculating the centroid from discrete image moments, given by Eq. 1.2 and Eq. 1.3, provides a more accurate, and faster, way of centring the scanned tip on the opposing tip. The centroid position after each scan is tracked as the intertip separation decreases from larger distances ($\sim 1 \mu\text{m}$) to around 100 nm as tips are brought into alignment. The centroids as a function of separation for a representative scan are shown in Figure 1.18.

Alignment is classified as the point at which the amplitude centroid is in agreement with the phase centroid. This criterion is chosen since the emergence of a peak in the phase signifies that the apex-apex capacitance dominates the response and because phase centroid does not deviate significantly from its initial position (Figure 1.18a,b). The amplitude centroid, on

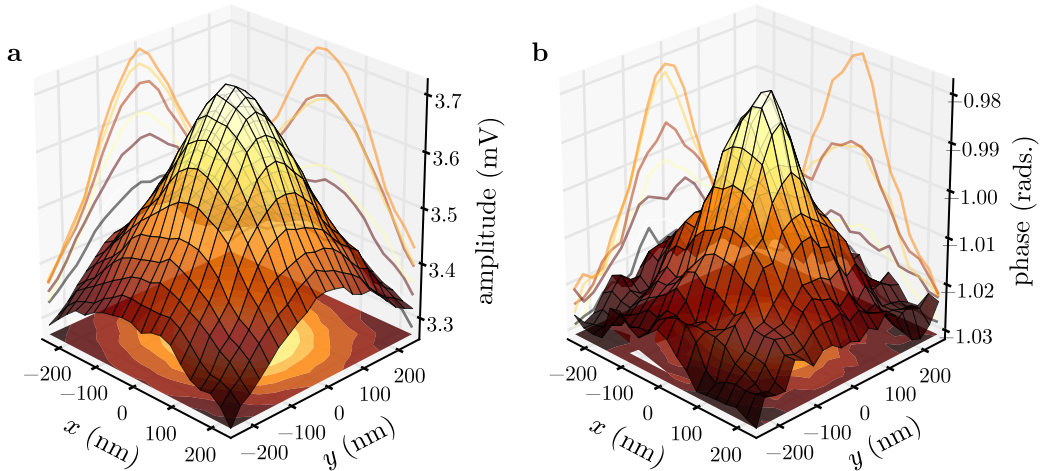


Figure 1.17: Alignment scan of a soft Au AFM tip scanned laterally over a stiff Au AFM tip. The soft tip is oscillating at 13 kHz (BudgetSensors ContGB) while the 300 kHz Au tip (BudgetSensors TapGB) remains static. Tips are separated by ~ 50 nm and driven at 8 V, remaining in the capacitively coupled regime. Strong peaks are seen in both the amplitude and the phase of the soft cantilever oscillation. The tips are aligned in a tip-to-tip configuration when both signals are maximised.

the other hand, follows the point of maximum capacitive coupling, which depends on the overall tip and cantilever shape, the separation regime and the driving voltage. For example, most pyramidal AFM tips are asymmetric in one direction with different opening angles from the apex, hence the point of maximum capacitance occurs when the higher angle tip facets overlap. As the separation decreases the apex-apex capacitance begins to dominate since the relative capacitance contributions to the amplitude go as d^{-2} , hence the fractional change in the intertip separation is far greater than the fractional change in the cantilever separation. Upon surpassing this point the asymmetry is effectively removed, as shown in Figure 1.18a,b.

The accuracy of the alignment can be quantified from the FWHM of both the amplitude and phase peaks. The FWHM of both centroids shortly after passing the alignment threshold constrict to a similar length. This is inevitably limited by the feature size of the tip apex, such as the radius of a sharp or spherical tip apex. When studying spherical tips with 150 nm radii the FWHM remains much larger since the surfaces in close proximity are much flatter in comparison. As the FWHM reduces the uncertainty on the centroid position reduces down to a few nanometres, well within the tolerance levels of any dual tip experiment.

Alignment using this technique is limited to conductive tips for best results. Tips necessarily have to be conductive to generate a strong capacitive signal at the tip junction. Most tips used with this technique have therefore been from Au or Pt AFM probes, though alignment of Si tips has been demonstrated at higher voltages since they are doped to dissipate static charge. Due to the improved signal quality when using optical detection compared to electronics, smaller oscillations can be used to align tips, which is good to maintain accuracy

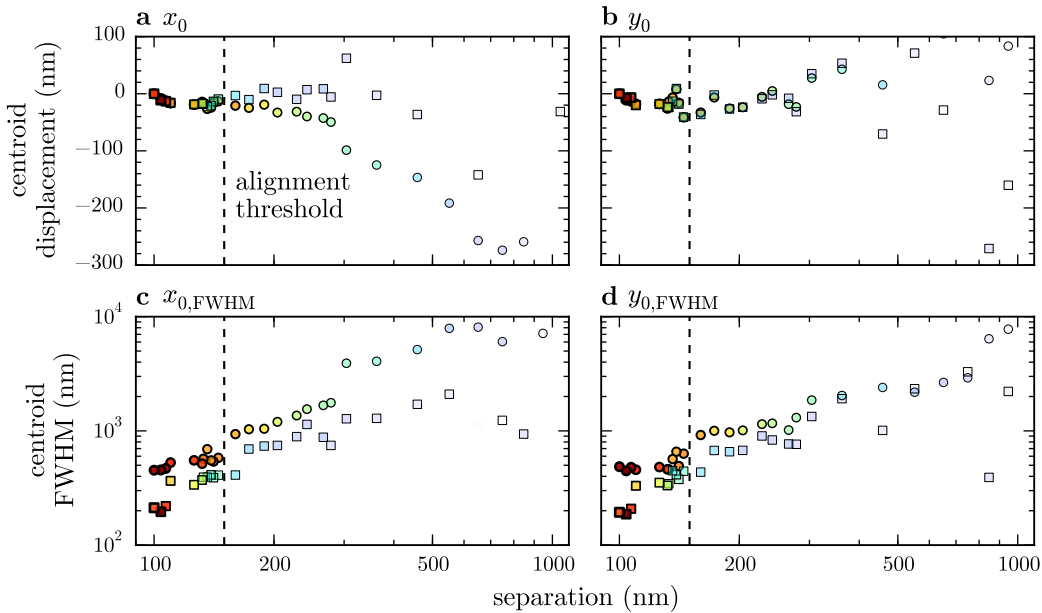


Figure 1.18: Centroid tracking during approach and alignment of two sharp Au tips. Amplitude (circles) and phase (squares) centroid positions relative to final alignment are shown in both the x (a) and y (b) directions. The centroid FWHM for the x and y amplitude and phase centroids are shown in (c) and (d), respectively. Marker colours indicate the strength of the peak in each alignment scan. A voltage of 8 V was maintained during each scan. The final separation is an order of magnitude estimate based on the eventual snap-in point and the onset of the tapping mode.

of alignment and reduce the risk of damaging tips. For a standard sharp Au tip dimer (one contact, one tapping mode cantilever) alignment has been carried out at voltages as low as 2 V for small tip separations. The PSD also offers at 400 kHz bandwidth compared with the 100 kHz bandwidth of available electronic lock-in amplifiers, allowing stiffer tips to be aligned on the occasion where a stiff dimer is needed. A demonstration of this high frequency alignment is shown in Figure 1.19 where a large voltage of 100 V was used to induce a sufficiently large oscillation for signal detection at 74 kHz.

To summarise, the capacitive alignment technique developed by Savage *et al.* [17] has been successfully adapted to use optical cantilever detection, as in AFMs, instead of direct electronic measurements of the tip junction. The technique is greatly improved, is less sensitive to other electronic systems integrated into the microscope, and has demonstrated the capability to align two tips to within a few nanometres of the target - less than the feature size of the tips. Both the frequency and spatial response have been studied, showing the tip separation dependence and the resulting alignment mechanism.

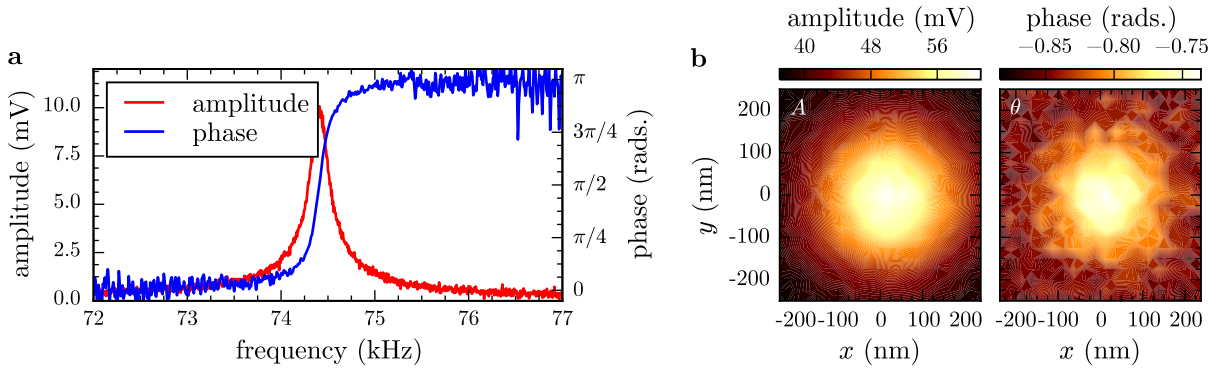


Figure 1.19: High frequency alignment data for a tip dimer composed of two 48 N m^{-1} Au AFM tips. Tips are separated by $\sim 50 \text{ nm}$ and driven at 120 V. (a) Frequency response of the system. (b) Amplitude and phase alignment scans showing the expected peaks as the moving tip scans over the stationary tip.

1.6 Conclusions

A custom-built ultra-stable microscope platform, utilising supercontinuum dark-field spectroscopy, low-noise electronics and AFM, is built to accommodate spectral studies of both individual tips and tip dimers. The platform is stable to both temperature and vibration and able to take two tips and align them into a dimer configuration using a modified form of scanning capacitance microscopy. Performance characterisation shows spectral validity between 500–1100 nm, more broadband than standard optical microscopes, with confocal localisation enabling the study of more complex structures than point scatterers. The addition of fA level current and AFM force measurements results in a system capable of characterising a sub-nm plasmonic dimer system in far more detail than ever before possible.

References

- [1] “Crc handbook of chemistry and physics”, in, edited by W. M. Haynes (CRC press, 2013).
- [2] R. H. Webb, “Confocal optical microscopy”, Reports on Progress in Physics **59**, 427 (1996).
- [3] D. B. Murphy, *Fundamentals of light microscopy and electronic imaging* (John Wiley & Sons, 2002).
- [4] G. Cox and C. J. Sheppard, “Practical limits of resolution in confocal and non-linear microscopy”, Microscopy research and technique **63**, 18–22 (2004).
- [5] O. Holzricher and W. Ibach, “High-resolution optical and confocal microscopy”, in *Confocal raman microscopy* (Springer, 2011), pp. 1–20.
- [6] M. Born and E. Wolf, *Principles of optics: electromagnetic theory of propagation, interference and diffraction of light* (Cambridge university press, 1999).
- [7] T. Wilson and A. Carlini, “Size of the detector in confocal imaging systems”, Optics letters **12**, 227–229 (1987).
- [8] J. L. Hutter and J. Bechhoefer, “Calibration of atomic-force microscope tips”, Review of Scientific Instruments **64**, 1868–1873 (1993).
- [9] T. Senden and W. Ducker, “Experimental determination of spring constants in atomic force microscopy”, Langmuir **10**, 1003–1004 (1994).
- [10] A. Torii et al., “A method for determining the spring constant of cantilevers for atomic force microscopy”, Measurement Science and Technology **7**, 179 (1996).
- [11] J. E. Sader, J. W. Chon, and P. Mulvaney, “Calibration of rectangular atomic force microscope cantilevers”, Review of Scientific Instruments **70**, 3967–3969 (1999).
- [12] R. Levy and M. Maaloum, “Measuring the spring constant of atomic force microscope cantilevers: thermal fluctuations and other methods”, Nanotechnology **13**, 33 (2002).
- [13] P. J. Cumpson, C. A. Clifford, and J. Hedley, “Quantitative analytical atomic force microscopy: a cantilever reference device for easy and accurate afm spring-constant calibration”, Measurement Science and Technology **15**, 1337 (2004).
- [14] R. S. Gates and M. G. Reitsma, “Precise atomic force microscope cantilever spring constant calibration using a reference cantilever array”, Review of Scientific Instruments **78**, 086101 (2007).
- [15] E. Langlois et al., “Spring constant calibration of atomic force microscopy cantilevers with a piezosensor transfer standard”, Review of Scientific Instruments **78**, 093705 (2007).

- [16] B. Ohler, “Cantilever spring constant calibration using laser doppler vibrometry”, *Review of Scientific Instruments* **78**, 063701 (2007).
- [17] K. J. Savage et al., “From microns to kissing contact: dynamic positioning of two nano-systems”, *Applied Physics Letters* **99**, 053110 (2011).
- [18] J. Matey and J Blanc, “Scanning capacitance microscopy”, *Journal of Applied Physics* **57**, 1437–1444 (1985).
- [19] C. Bugg and P. King, “Scanning capacitance microscopy”, *Journal of Physics E: Scientific Instruments* **21**, 147 (1988).
- [20] Y Huang, C. Williams, and J Slinkman, “Quantitative two-dimensional dopant profile measurement and inverse modeling by scanning capacitance microscopy”, *Applied physics letters* **66**, 344–346 (1995).
- [21] J. Kopanski, J. Marchiando, and J. Lowney, “Scanning capacitance microscopy measurements and modeling: progress towards dopant profiling of silicon”, *Journal of Vacuum Science & Technology B* **14**, 242–247 (1996).
- [22] P. Girard, “Electrostatic force microscopy: principles and some applications to semiconductors”, *Nanotechnology* **12**, 485 (2001).
- [23] J. Tamayo and R Garcia, “Deformation, contact time, and phase contrast in tapping mode scanning force microscopy”, *Langmuir* **12**, 4430–4435 (1996).
- [24] R. Garcia and A. San Paulo, “Attractive and repulsive tip-sample interaction regimes in tapping-mode atomic force microscopy”, *Physical Review B* **60**, 4961 (1999).
- [25] A. San Paulo and R. Garcia, “Unifying theory of tapping-mode atomic-force microscopy”, *Physical Review B* **66**, 041406 (2002).
- [26] S. Lee et al., “Nonlinear dynamics of microcantilevers in tapping mode atomic force microscopy: a comparison between theory and experiment”, *Physical Review B* **66**, 115409 (2002).